J. Fluid Mech. (2021), *vol*. 922, A21, doi:10.1017/jfm.2021.558

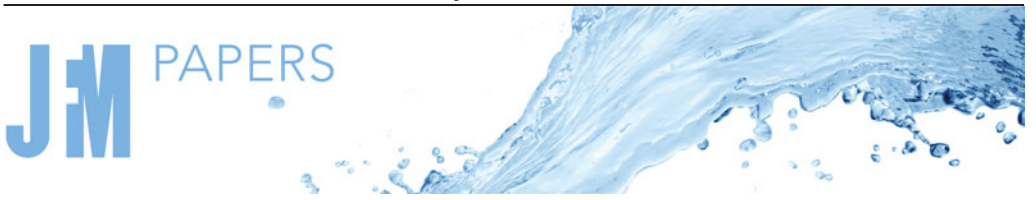

Efficient aquatic locomotion using elastic propulsors with hybrid actuation

Ersan Demirer[1], **Oluwafikayo A. Oshinowo**[2] **and Alexander Alexeev**[1],†

[1]George W. Woodruff School of Mechanical Engineering, Georgia Institute of Technology, Atlanta, GA 30332, USA

[2]Daniel Guggenheim School of Aerospace Engineering, Georgia Institute of Technology, Atlanta, GA 30332, USA

(Received 27 February 2021; revised 24 April 2021; accepted 17 June 2021)

Using computational modelling, we probe the hydrodynamics of a bio-inspired elastic propulsor with hybrid actuation that oscillates at resonance in a Newtonian fluid. The propulsor is actuated by a heaving motion at the base and by an internal bending moment distributed along the propulsor length. The simulations reveal that by tuning the phase difference between the external and internal actuation, the propulsor thrust and free-swimming velocity can be regulated in a wide range while maintaining high efficiency. Furthermore, the hybrid propulsor outperforms propulsors with either of the actuation methods. The enhanced performance is associated with the emerging bending pattern maintaining large tip displacement with reduced centre-of-mass displacement. The results are useful for developing highly efficient robotic swimmers utilizing smart materials as propulsors with simplified design and operation.

Key words: swimming/flying, propulsion, flow-structure interactions

1. Introduction

The pursuit of more effective means of aquatic locomotion has compelled researchers and engineers to tackle the fluid–structure interaction problem of fish swimming (Combes & Daniel 2001; Chen, Shatara & Tan 2009; Liu & Aono 2009; Kolomenskiy *et al.* 2011; Alben *et al.* 2012). While current man-made designs generally rely on rigid propulsors to move through a fluid, nature widely harnesses elasticity for aquatic locomotion (Jayne & Lauder 1995; McHenry, Pell & Long 1995; Lauder & Tytell 2005; Fish & Lauder 2006). For instance, fish use their muscles to actively change the shape and stiffness of their bodies in order to swim and manoeuvre (Wardle, Videler & Altringham 1995; Ramananarivo, Godoy-Diana & Thiria 2013; Pabst 2015). Fish hydrodynamic performance

† Email address for correspondence: alexander.alexeev@me.gatech.edu

is intrinsically characterized by the two-way coupling between the deformation of the fish body and the fluid flow. This complex interplay between solid and fluid motion enables fish to exhibit unmatched swimming velocities, manoeuvrability and efficiency.

Multiple experimental studies have explored bio-inspired designs of varying complexity as prototypes for underwater swimmers (Yu *et al.* 2004; Hu *et al.* 2006; Philen & Neu 2011; Marras & Porfiri 2012; Kopman *et al.* 2015). The earliest designs of robotic fish used complex networks of strings and servomotors to replicate the tail motion typically encountered in carangiform swimming modes (Triantafyllou & Triantafyllou 1995; Anderson *et al.* 1998). More recent designs include a series of linked sections coupled to actuators (Flammang & Lauder 2009; Esposito *et al.* 2012; Su *et al.* 2014; Lauder & Tangorra 2015). These locomotion approaches share a common actuation method relying on a form of heaving or pitching motion imposed at the propulsor base. We refer to this method of actuation as the external actuation. Numerous experimental and numerical studies have also explored the hydrodynamics of propulsors with a combination of heaving and pitching actuation. For instance, Piñeirua, Thiria & Godoy-Diana (2017), Smits (2019), Van Buren, Floryan & Smits (2019) and Quinn, Lauder & Smits (2015) investigated the impact of introducing a phase lag between a heaving and pitching actuation. The authors showed that the phase lag is a critical parameter to maximize the efficiency of the propulsor. Nevertheless, such actuation requires a high level of control of the base motion to enable complex multidimensional biomimetic propulsion, imposing constraints in terms of propulsor implementation and cost.

Research shows that the elasticity plays a critical role in biomimetic locomotion. Using experiments and modelling, Alben *et al.* (2012) demonstrated the existence of resonance peaks in the free-swimming velocity of an elastic oscillating plate. The model predicted that the plate velocity is proportional to the plate length to the power of $-1/3$ and to plate flexibility to the power of $2/15$. Dai *et al.* (2012) showed that an elastic plate generates significantly more thrust than a rigid plate at the same Strouhal number. Using experiments, Quinn, Lauder & Smits (2014) demonstrated that the resonance peaks in free-swimming velocity occur for discrete values of the effective flexibility, defined as a ratio of the added mass and bending forces. Hoover *et al.* (2018) further confirmed these findings with three-dimensional simulations of free-swimming flexible plates. Yeh & Alexeev (2014) used fully coupled three-dimensional simulations to show that elastic propulsors could be operated at a regime of maximum propulsion near the first natural frequency or maximum efficiency away from the resonance.

Recent progress in smart materials makes it possible to overcome certain shortcomings and limitations in designing biomimetic propulsors (Wang *et al.* 2008; Chen *et al.* 2009, 2011; Chu *et al.* 2012). Among different smart materials, internally actuated macro-fibre composites (MFCs) offer a balance between actuation control and deformation levels, as well as reduced design complexity and silent operation (Heo *et al.* 2007; Cen & Erturk 2013). MFC bimorph actuation is a result of a distributed internal moment due to the contraction of two MFCs bonded by a layer of epoxy. We refer to this method of actuation as internal actuation. While such smart materials are highly attractive for use in biomimetic locomotion, previous research has indicated that internally actuated propulsors underperform in terms of thrust and efficiency when compared to externally actuated propulsors (Yeh & Alexeev 2016*a*; Demirer *et al.* 2021). The deficiency of the internal actuation is linked to a suboptimal bending pattern of such propulsors with a characteristic cupping of the actuator tip, which increases viscous losses. This leads to the question of whether a hybrid actuation that uses a combination of external and internal actuation can yield superior hydrodynamics, outperforming either of these actuation

methods while offering a high degree of control over the bending pattern and propulsion characteristics.

In this work, we use fully coupled three-dimensional simulations to probe the hydrodynamics of an elastic plate propulsor actuated at resonance by combined external and internal actuation representative of a heaving MFC bimorph. We examine the effects of a phase lag between the externally imposed heaving motion at the propulsor base and the internal distributed bending moment on the propulsor hydrodynamics. We consider hybrid propulsors in constrained and free-swimming configurations. In the former configuration the plate is constrained from moving forward at its base, whereas in the latter configuration the plate can swim freely. Our simulations indicate that the hybrid actuation results in a synergistic relationship between the internal and external actuation that dramatically enhances the hydrodynamic performance of the plate propulsor.

2. Methodology

We consider a bio-inspired elastic propulsor with hybrid actuation that is driven by a combination of external and internal actuation to oscillate in an incompressible Newtonian fluid with density ρ and dynamic viscosity μ. The propulsor is represented by a thin elastic plate of length L, width w and thickness $h \ll L$, leading to an aspect ratio of $\mathcal{A}_\mathcal{R} = L/w = 2.5$ (figure 1*a*). The plate bending stiffness is D, the mass density is ρ_s and the mass ratio is $\chi = \rho w/\rho_s h = 10$. The external actuation is imposed at the plate base, leading to time-periodic heaving base oscillations $a(t) = A_0 L \sin(\omega t)$, where A_0 is the dimensionless heaving amplitude. The plate internal actuation is due to a time-periodic bending moment $m(t) = M_0 D(L/w) \sin(\omega t + \phi)$, where M_0 is the dimensionless moment amplitude and ϕ is the phase lag between the external and internal actuation (figure 1*b*). This time-varying bending moment is imposed at the free end of the plate through a local force couple. Note that M_0 represents the magnitude of the static tip deflection of the plate due to the bending moment normalized by the plate length. Practically, the internal actuation represents the behaviour of an MFC piezoelectric plate (Yeh & Alexeev 2016*a*; Demirer *et al.* 2021). Here, a local bending moment is generated by bonding two MFCs with a layer of epoxy and applying opposite currents to the two MFCs (Tan & Erturk 2018). Among different smart materials, MFCs strike an attractive balance between actuation and displacement levels, as well as providing silent operation. The external and internal actuations share the same angular frequency $\omega = 2\pi/\tau$, with τ being the actuation period. We set $\omega = \omega_{res}$, with ω_{res} being the fundamental resonance frequency of the plate in fluid (Weaver, Timoshenko & Young 1990), leading to a Reynolds number of $Re = \rho u_c L/\mu = 1000$, where $u_c = L/\tau$ is the characteristic velocity. The corresponding plate stiffness D leads to the Cauchy number $C_y = \rho u_c^2 L^3/D = 0.065$, which relates the fluid loading to the plate elasticity. To explore the hydrodynamics of combined actuation, we fix the external actuation amplitude as $A_0 = 0.1$ while varying the internal moment amplitude M_0 and the phase lag ϕ.

In the constrained configuration, the plate oscillates in a quiescent fluid, and its base is kept in place in the x-direction (figure 1*c*). The hydrodynamics of the constrained plate is characterized in terms of the dimensionless period-averaged thrust $F_x = f_x/f_c$, power $\mathcal{P} = p/p_c$ and efficiency $\eta_c = f_x u_c/p$. Here, $f_c = \frac{1}{2}\rho u_c^2 wL$ is the characteristic force, and $p_c = f_c u_c$ is the characteristic power. The instantaneous power is computed by integrating over the plate surface the dot product of the hydrodynamic forces and the local velocity. In the free-swimming configuration, the plate is free to propel through the fluid in the x-direction. In this configuration the total drag and thrust acting on the plate balance each

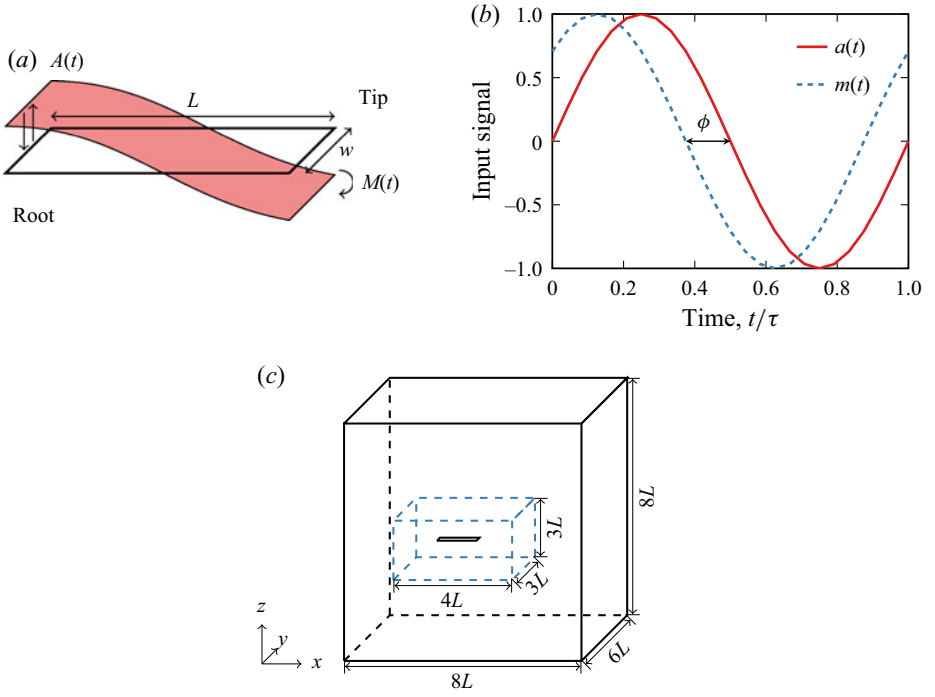

Figure 1. (*a*) Schematic of an oscillating elastic plate with length L, width w and thickness $h \ll L$. The plate is actuated by a heaving motion at the base $a(t)$ and by a distributed internal bending moment $m(t)$. (*b*) Plate actuation signals with a phase lag ϕ. (*c*) Simulation domain consists of a coarse outer mesh and a fine inner mesh around the oscillating solid plate at the centre.

Metric	Constrained	Free-swimming
Propulsion	$F_r = 0.221$	$U_r = 0.6$
Power	$\mathcal{P}_r = 1.276$	$\mathcal{P}_r = 1.136$
Efficiency	$\eta_{r,c} = 0.173$	$\eta_{r,f} = 0.715$

Table 1. Swimming characteristics of the reference externally actuated elastic plate with $A_0 = 0.1$.

other, leading to a net zero period-averaged hydrodynamic force. The free swimming is characterized by the dimensionless period-averaged swimming velocity $U = u/u_c$, power $\mathcal{P} = p/p_c$ and efficiency $\eta_f = uf_c/p$.

To characterize and compare the performance of propulsors with different actuation methods, we use an externally actuated plate at resonance with $A_0 = 0.1$ as a reference configuration. The characteristics of constrained and free-swimming propulsors are normalized by the respective values for the constrained and free-swimming reference propulsors. Table 1 provides the values of the relevant hydrodynamic characteristics for the reference propulsor configurations.

We model plate oscillations in a viscous fluid using a fully coupled fluid–structure interaction framework integrating a lattice Boltzmann (LB) model and a finite differences model (Demirer *et al.* 2021). The computational domain is fitted with a cubic lattice of equally spaced nodes with higher grid density near the oscillating plate, as shown

in figure 1(*c*). The flow is characterized by a velocity distribution function $g_i(\boldsymbol{r}, t)$ representing the density of fluid at position $\boldsymbol{r}$ that is propagating along the lattice direction i with velocity $\boldsymbol{c}$ at time t. We use a D3Q19 lattice that maintains 19 velocity directions in the three-dimensional space. We integrate the discrete Boltzmann equation to calculate the time evolution of the distribution function $g_i(\boldsymbol{r}, t)$ and retrieve relevant macroscopic quantities by taking moments of the distribution function (Ladd & Verberg 2001).

We set $\rho = 1$, $\mu = 1.25 \times 10^{-3}$ and $\tau = 2000$ in LB units. The fine and coarse fluid grids, respectively, measure $4L \times 3L \times 3L$ and $8L \times 6L \times 8L$, where $L = 50$ LB units. The fine and coarse node spacing are, respectively, $\Delta_f = 1$ and $\Delta_c = 2$ in LB units. The plate is discretized with 21 nodes in the length and 11 nodes in the width, so that $\Delta_x = 2.381$ and $\Delta_y = 1.82$ in LB units. Further details and validation of our computational framework can be found elsewhere (Masoud & Alexeev 2010, 2012; Mao & Alexeev 2014; Yeh & Alexeev 2014; Yeh, Li & Alexeev 2017; Yeh, Demirer & Alexeev 2019; Demirer *et al.* 2021).

3. Results and discussion

Figure 2(*a*) shows the variation of the normalized thrust F_x/F_r for the constrained plate and the normalized swimming velocity U/U_r for the free-swimming plate with the phase ϕ. We find that these two propulsion metrics are strongly correlated, indicating that either can be used to characterize the plate propulsion. This correlation suggests that, with relation to their respective reference configurations (the constrained and free-swimming externally actuated plates), the hybrid actuation dependence on ϕ is similarly proportional for the thrust and swimming velocity. The propulsion is maximized when the external actuation and the internal actuation are nearly in phase at $\phi = \pi/12$, and is minimized when the actuation signals are in phase opposition about $\phi = 11\pi/12$. Compared to the externally actuated reference case, the combined actuation with $M_0 = 0.1$ doubles the propulsion, whereas using $M_0 = 0.05$ increases the propulsion by about 50 %. The propulsion with combined actuation increases to nearly 7.7 times that of the reference case with $M_0 = 0.4$ (see the inset in figure 2*a*). For $M_0 > 0.4$ the free end cupping negatively affects the swimming performance of combined actuation, decreasing the propulsion. When the plate is actuated out of phase, the combined actuation can reduce the propulsion to nearly zero. Note that the propulsion is not symmetric with respect to $\phi = 0$ or $\phi = \pi$. At $\phi = \pi/2$, $F_x/F_r \simeq 1$, while at $\phi = 3\pi/2$, $F_x/F_r \simeq 1.28$, which is a 28 % difference. Note also that the internal actuation alone with, respectively, $M_0 = 0.1$ and $M_0 = 0.05$ yields propulsion that is only about 50 % and 10 % of that of the externally actuated plate. Thus, the combined actuation not only enables wide control over the propulsion, but can yield propulsion that significantly exceeds the sum of the propulsion of the plates with separate external and internal types of actuation.

As shown in figure 2(*b*), the power exhibits a dependence on ϕ that is similar to that of the propulsion. The power is maximized at $\phi = \pi/6$ and minimized at $\phi = \pi$. The maximum power of the plate with combined actuation significantly exceeds the cumulative power of plates with separate external and internal actuation. Furthermore, combined actuation can greatly reduce $\mathcal{P}$ compared to external actuation alone. Similarly to the propulsion, the power is not symmetric with respect to $\phi = 0$ or $\phi = \pi$. At $\phi = \pi/2$, $\mathcal{P}/\mathcal{P}_r \simeq 1.49$, while at $\phi = 3\pi/2$, $\mathcal{P}/\mathcal{P}_r \simeq 1.2$, which corresponds to a nearly 20 % difference in power. We attribute this symmetry-breaking to nonlinear effects arising from the large deformation of the plate actuated with the hybrid actuation method.

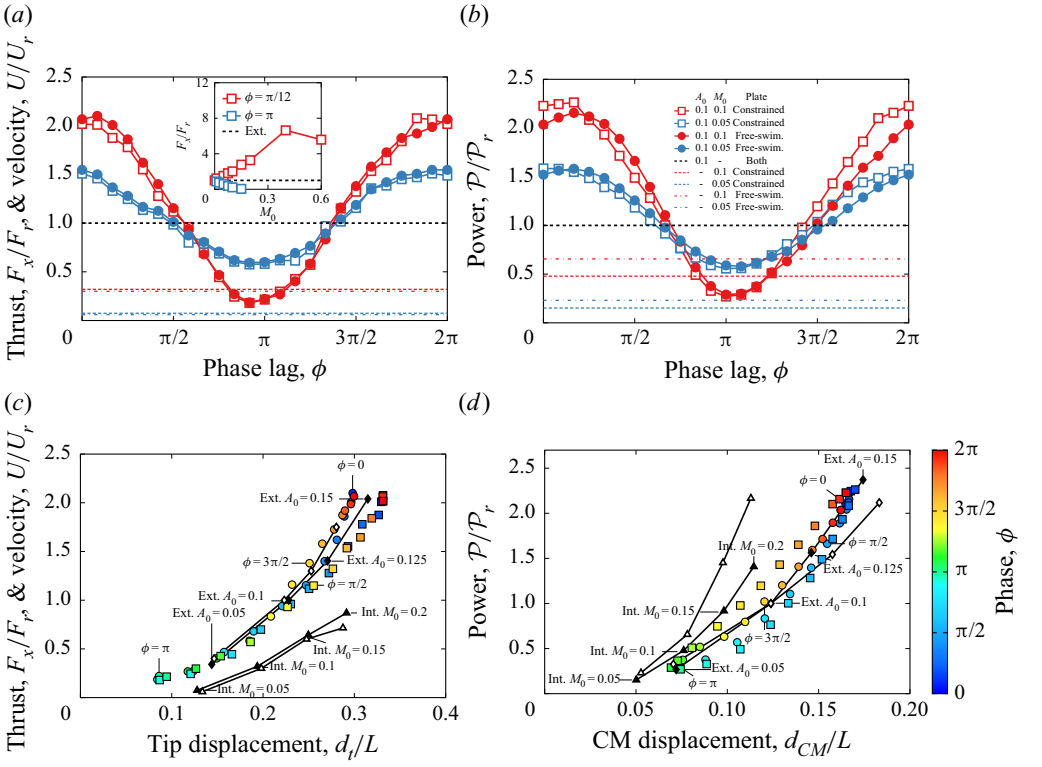

Figure 2. (*a*) Normalized thrust F_x/F_r and velocity U/U_r as functions of the phase difference between the internal and external actuation ϕ. The inset shows the maximum and minimum values of F_x/F_r as a function of M_0. (*b*) Normalized power $\mathcal{P}/\mathcal{P}_r$ as a function of ϕ. The horizontal dashed lines in (*a*) and (*b*) show the propulsion for internally actuated plates with $M_0 = 0.1$ (red lines) and $M_0 = 0.05$ (blue lines). The dashed lines show the thrust, while the dash-dotted lines show the velocity. (*c*) Dependence of the thrust F_x and velocity U on the amplitude of the tip displacement d_t for $M_0 = 0.1$. (*d*) Dependence of the power $\mathcal{P}$ on the amplitude of the plate's centre-of-mass displacement d_{CM} for $M_0 = 0.1$. In (*c*) and (*d*), the coloured circles and squares show, respectively, the combined actuation data for free-swimming and constrained configurations, with the colours indicating the phase lag ϕ. The solid lines with symbols in (*c*) and (*d*) show the constrained external (filled diamonds), free-swimming external (empty diamonds), constrained internal (filled triangles) and free-swimming internal (empty triangles) actuation methods with different amplitudes of A_0 and M_0.

The trailing-edge displacement d_t is a major parameter that controls the plate propulsion (Michelin & Llewellyn Smith 2009). Figure 2(*c*) shows the propulsion metrics as functions of d_t (see figure 1 of the supplementary material, available at https://doi.org/10.1017/jfm.2021.558, for the dependence of d_t on ϕ). We find that there is a direct relationship between the velocity and thrust data and the trailing-edge displacement. The data for externally actuated plates with varying actuation amplitudes in the free-swimming and constrained configurations closely match the results for the propulsors with combined actuation. On the other hand, free-swimming and constrained internally actuated plates with varying M_0 yield significantly lower performance than the combined actuation for comparable tip displacement. This is consistent with previous results (Demirer *et al.* 2021) and can be attributed to the suboptimal bending pattern of internally actuated plates. Thus, in the case of combined actuation, the phase ϕ controls the tip displacement, which in turn defines the propulsion characteristics. Note that with the combined and external actuation

methods, U/U_r in the free-swimming configuration increases slightly faster than F_x/F_r in the constrained configuration with increasing d_t. Furthermore, the free-swimming configuration results in somewhat smaller d_t than the constrained configuration, which is related to an increased added mass effect due to the incoming fluid flow. Indeed, the incoming flow imposes an additional restoring force to the plate, which in turn increases the effective stiffness and lowers d_t (Yeh & Alexeev 2014).

As shown in figure 2(d), the power $\mathcal{P}$ scales with the displacement of the plate's centre of mass d_{CM} (see figure 1 in the supplementary material for the dependence of d_{CM} on ϕ). The power consumption is minimized with the reduced centre-of-mass displacement and gradually increases with increasing d_{CM}. The plates with the combined actuation and the external actuation show similar dependencies, whereas the internally actuated plate requires a slightly greater power for the same centre-of-mass deflection. Note that d_t and d_{CM} for the plates with combined actuation are maximized when the external and internal actuation act in phase, $\phi = \pi/12$, and minimized when they are in phase opposition, $\phi = \pi$.

In figure 3(a) we show the efficiencies η_c and η_f for, respectively, constrained and free-swimming plates with combined actuation. Both these parameters reveal a similar dependence on ϕ. More importantly, the efficiency can significantly exceed the value characterizing the plate with the external actuation. The maximum efficiency of the combined actuation is about 25 % greater than that of the external actuation. The phase difference $\phi = 4\pi/3$ leading to this actuation regime is nearly independent of M_0. The enhancement of the efficiency is maximized when $M_0 \simeq 0.075$, as shown in the inset in figure 3(a). When $M_0 < 0.04$, the efficiency decreases below the reference value. In this M_0 range, the increased power due to the internal actuation outweighs its benefit for the propulsion. For greater M_0, the internal actuation translates into a significant increase of the plate efficiency, up to $M_0 \simeq 0.1$. Further increase of M_0 yields less efficient propulsion because of the tip cupping.

Note that the phase of the maximum thrust and the maximum velocity, $\phi = \pi/12$, does not match the phase of the maximum efficiency, $\phi = 4\pi/3$. Thus, the maximum propulsion is achieved at the cost of reduced efficiency. Furthermore, the combined actuation with $M_0 = 0.4$ that yields the overall maximum thrust $F_x/F_r \simeq 7.7$ at $\phi = \pi/12$ (figure 2a) has a reduced efficiency of $\eta_c/\eta_{r,c} \simeq 0.86$, whereas at $\phi = 4\pi/3$ the thrust is $F_x/F_r \simeq 2$ and the efficiency is $\eta_c/\eta_{r,c} \simeq 0.98$.

The efficiency represents the ratio of the propulsion metrics and the power. Since the propulsion and the power scale with, respectively, d_t and d_{CM}, in figure 3(b) we plot η_c and η_f as functions of d_{CM}/d_t. Indeed we find that the data for the plates with combined actuation cluster closely, showing a decreasing trend with increasing d_{CM}/d_t. Thus, for efficient propulsion, the bending pattern needs to have low d_{CM} and high d_t, whereas plate oscillations in which d_{CM} increases with respect to d_t result in less efficient propulsion. For plates with independent internal and external actuation, we find that d_{CM}/d_t changes only slightly with the amplitude, since at resonance the bending patterns weakly depend on the oscillation amplitude.

Note that for the plates with internal actuation only, d_{CM}/d_t is relatively small compared to the value for externally actuated plates, and about the same as the lowest d_{CM}/d_t obtained with hybrid actuation. Nevertheless, these propulsors show low efficiency due to the suboptimal tip bending. Thus, having low d_{CM}/d_t is insufficient for efficient locomotion. In the inset in figure 3(b), we show the efficiency as a function of the ratio θ/β between the tip angle at the maximum velocity θ and the base angle $\beta = \arctan(\omega A_0 L/U)$ (Ramananarivo, Godoy-Diana & Thiria 2011) (see figure 2 in the

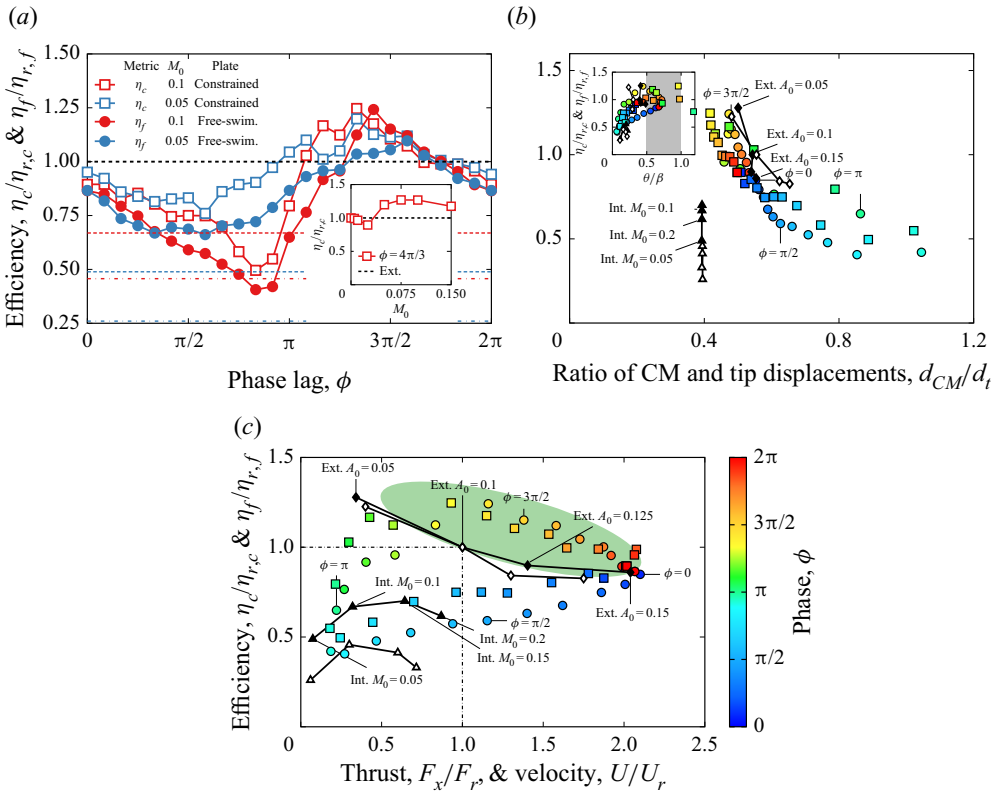

Figure 3. (*a*) Normalized constrained efficiency $\eta_c/\eta_{c,r}$ and free-swimming efficiency $\eta_f/\eta_{f,r}$ as functions of the phase difference ϕ. The inset shows the maximum efficiency as a function of M_0. The horizontal lines show the efficiency for internally actuated plates with $M_0 = 0.1$ (red lines) and $M_0 = 0.05$ (blue lines). (*b*) Dependence of the efficiencies η_c and η_f on the ratio between the centre-of-mass and tip deflections, d_{CM}/d_t, for $M_0 = 0.1$. The inset shows the efficiency as a function of θ/β. (*c*) Dependence of the efficiencies η_c and η_f on the thrust F_x and velocity U for $M_0 = 0.1$. In (*b*) and (*c*), the coloured circles and squares show, respectively, the combined actuation data for free-swimming and constrained configurations, with the colours indicating the phase lag ϕ. The solid lines with symbols in (*b*) and (*c*) show the constrained external (filled diamonds), free-swimming external (empty diamonds), constrained internal (filled triangles) and free-swimming internal (empty triangles) actuation methods with different amplitudes of A_0 and M_0.

supplementary material). In the constrained configuration, the plate oscillates in quiescent fluid; therefore we approximate the cruising velocity U by the tip velocity V_t, which yields $\beta = \arctan(\omega A_0 L/V_t)$.

For efficient swimming, θ/β should be between 0.5 and 1 (Ramananarivo *et al.* 2011). We find that the externally actuated plates and the plates with hybrid actuation with higher efficiency are indeed close to the range of efficient θ/β. The internally actuated plates, on the other hand, have values of θ/β that are much lower than the optimum range, confirming that the low efficiency is due to the bending pattern with a suboptimal tip angle. In the free-swimming configuration, $\theta/\beta > 1$ leads to flow separation and increased drag, which negatively affects the energetic performance. Although a direct translation between the stationary and free-swimming cases is not expected, we find good agreement with this criterion in both instances. When the propulsor is stationary, the magnitude of the local flow velocity induced by the plate is estimated to be about that of the plate tip velocity.

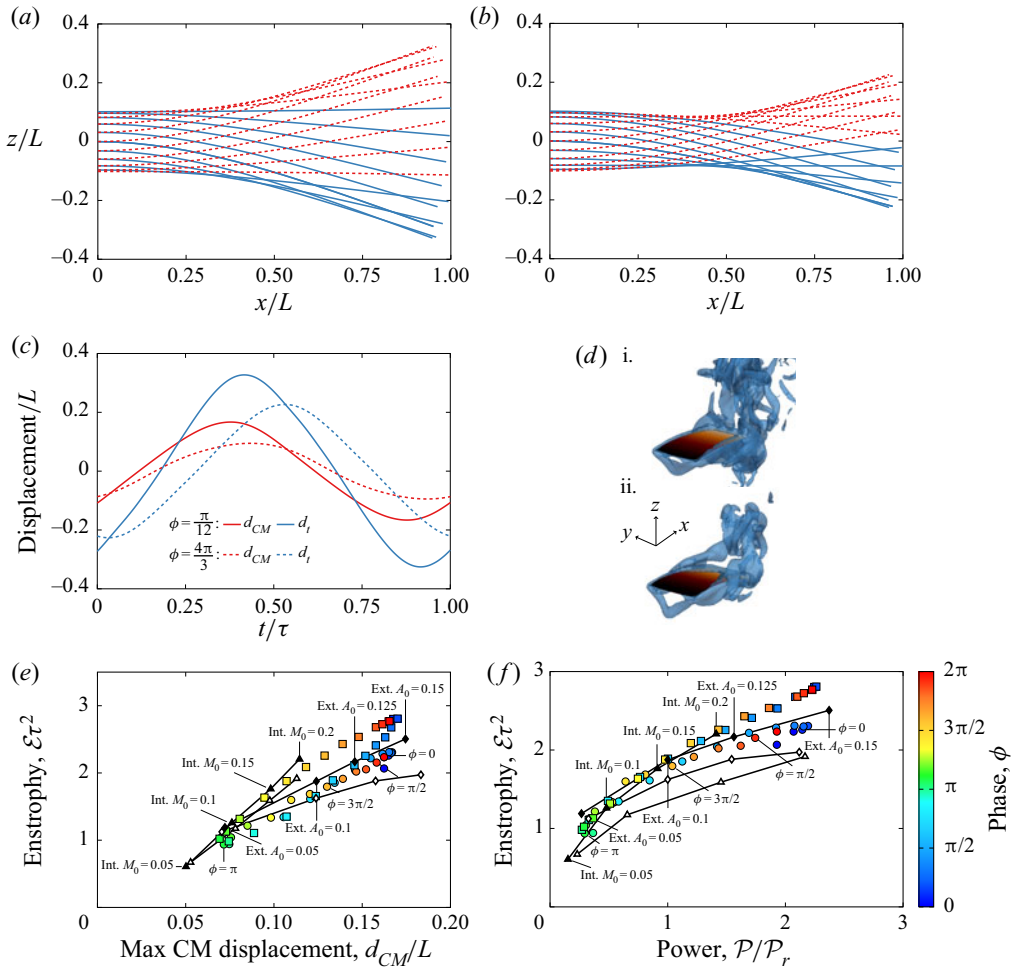

Figure 4. (*a*) Bending pattern of a plate with combined actuation at the maximum thrust ($\phi = \pi/12$). (*b*) Bending pattern of a plate with combined actuation at the maximum efficiency ($\phi = 4\pi/3$). The solid blue lines and the dashed red lines in (*a*) and (*b*) correspond to the plate profiles during the upstroke and downstroke, respectively. (*c*) Time histories of the tip displacement d_t and the centre-of-mass displacement d_{CM} at the maximum efficiency and the maximum thrust. (*d*) Contours of the normalized vorticity $\omega\tau = 10$ for (i) the maximum thrust and (ii) the maximum efficiency (see movie 1 in the supplementary material). (*e*) Dependence of the enstrophy $\mathcal{E}$ on the maximum centre-of-mass displacement d_{CM}. (*f*) Dependence of the enstrophy $\mathcal{E}$ on the power $\mathcal{P}$. In (*e*) and (*f*), the coloured circles and squares show, respectively, the combined actuation data for free-swimming and constrained configurations, with the colours indicating the phase lag ϕ. The solid lines with symbols in (*e*) and (*f*) show the constrained external (filled diamonds), free-swimming external (empty diamonds), constrained internal (filled triangles) and free-swimming internal (empty triangles) actuation with different amplitudes of A_0 and M_0.

We find that similarly to the free-swimming case, an exceedingly large magnitude of θ/β is detrimental to propulsion performance, because of increased dissipation.

Overall, the propulsor performance is enhanced when both the efficiency and propulsion are maximized. In figure 3(*c*) we show the relationship between the efficiency and the propulsion. For the plate with the external actuation, the efficiency decreases with increasing propulsion. Thus, one needs to compromise by maximizing either the propulsor's efficiency or its propulsion. Although the internally actuated plate performs

poorly compared to the plate with external actuation, the plate with a combination of external and internal actuation yields a propulsor that significantly outperforms the externally actuated plate in terms of both characteristics simultaneously, as indicated by the green ellipse in figure 3(*c*). The combined actuation surpasses the externally actuated propulsor in both propulsion and efficiency in a wide range of $3\pi/2 < \phi < 2\pi$. Note that the maximum propulsion at $\phi = \pi/12$ is characterized by higher efficiency than an equivalent propulsion level achieved by the external actuation with an increased actuation amplitude. The combined actuation yields up to 60 % greater propulsion for the same efficiency and is 25 % more efficient for the same propulsion output than the external actuation.

In figure 4, we examine the bending pattern and the hydrodynamics of plates with combined actuation at the maximum efficiency ($\phi = 4\pi/3$) and the maximum propulsion ($\phi = \pi/12$) (see also figure 3 in the supplementary material for additional values of ϕ). At the maximum propulsion, the plate exhibits a typical bending pattern for actuation at resonance that maximizes the tip deflection (figure 4*a*). At the maximum efficiency, the bending pattern develops a dip near the middle of the plate, reducing the displacement of the centre of mass (figure 4*b*). Note that the bending pattern at $\phi = \pi/12$ is similar to that of an externally actuated plate, whereas the internally actuated plate shows a distinctly different pattern with no displacement at the root and non-vanishing curvature at the tip (Demirer *et al.* 2021) (see figure 4 in the supplementary material).

The tip and centre-of-mass displacements over an oscillation period are shown in figure 4(*c*). At $\phi = \pi/12$, the tip and centre of mass move by nearly 50 % more than at $\phi = 4\pi/3$. In terms of the phase lag between the tip and actuation signals, φ, our simulations show that in the regime of maximum efficiency, the tip and actuation are in phase quadrature, as is characteristic of resonance oscillations, whereas at the maximum efficiency the phase is $\varphi \simeq 2\pi/3$. This confirms that the combined actuation modulates φ and, therefore, the bending mode (see figure 5 in the supplementary material).

We use the mean enstrophy $\mathcal{E}$ to quantify the vorticity generated by the plates (Demirer *et al.* 2021). We find that $\mathcal{E}$ roughly scales with d_{CM} (figure 4*e*), indicating that the magnitude of centre-of-mass displacement dictates to a large extent the amount of vorticity produced by the plate. The plates with solely internal or solely external actuation generate $\mathcal{E}$ similar to that of the combined actuation plate. Furthermore, when $\mathcal{E}$ is plotted against the power $\mathcal{P}$ (figure 4*f*), we find that the data for all actuation methods collapse into a single curve. Thus, the power indeed scales with the amount of enstrophy, which in turn is defined by the centre-of-mass displacement. Interestingly, the enstrophy is sensitive to the plate configuration. Free-swimming plates generate significantly less enstrophy than constrained plates for comparable power $\mathcal{P}$, when $\mathcal{P}$ is sufficiently large. This holds for combined, external and internal actuation.

4. Conclusions

We have shown that the hybrid internal–external actuation can be used to regulate the hydrodynamic performance of a propulsor by changing the phase difference between the actuation methods while maintaining high efficiency, outperforming propulsors with a single actuation method. Our results suggest that the propulsion scales with the magnitude of the tip displacement, whereas the power scales with the displacement of the centre of mass of the propulsor. The hybrid actuation provides a unique way to regulate the balance between these two metrics, thereby yielding an efficient propulsor with

superior performance. These findings indicate that energy dissipation is mostly associated with vortex generation and side-edge vortices, whereas the propulsion is controlled by the trailing-edge vortices, which is consistent with previous studies on flexible propulsors (Dai *et al.* 2012; Quinn *et al.* 2014; Raspa *et al.* 2014; Yeh & Alexeev 2016*b*; Li, Liu & Su 2017). The hybrid propulsor performance is analysed in a constrained configuration, where the propulsor oscillates in a quiescent fluid and its base is kept from moving forward, and in a free-swimming configuration, where the propulsor can freely propel forward through the fluid. Our simulations show that the hydrodynamic performance in these two configurations is closely correlated, although in free swimming, the propulsor exhibits a slightly lower trailing-edge displacement due to the effect of upcoming fluid flow.

Our results are also useful for developing biomimetic propulsors with other modes of combined actuation, such as propulsors using a combination of heaving and pitching root actuation. Such propulsors have been the subject of numerous studies indicating that the angle of attack and the phase lag between the heaving and pitching are critical parameters to maximize the efficiency (Quinn *et al.* 2015; Piñeirua *et al.* 2017; Smits 2019). In particular, it has been shown that the thrust is maximized at the phase difference $11\pi/6$, the power is minimized at $7\pi/6$ and the efficiency is maximized at $3\pi/2$ (Van Buren *et al.* 2019), which are close to the respective phases identified for the hybrid internal–external actuation.

Macro-fibre composite (MFC) piezoelectric materials are particularly attractive for designing active propulsors with combined actuation because of their robustness and high efficiency (Sodano 2003; Williams, Inman & Wilkie 2006; Cen & Erturk 2013). In this case, the base of the MFC propulsor can be actuated using a mechanical system similar to those used in current designs (Mason & Burdick 2000; Yan *et al.* 2008; Wu *et al.* 2015), whereas the piezoelectric actuation can be harnessed to impose a time-periodic internal bending moment dynamically modulating the propulsor shape. Active propulsors, such as those made of MFC piezoelectric materials, are especially promising for the design of small-scale robotic swimmers, because they offer reduced mechanical complexity, ease of integration and operational control (Tan & Erturk 2018). We note that our simulations point to the superior hydrodynamic efficiency of propulsors with combined actuation. In practice, additional energy losses associated with the driving and control mechanisms need to be accounted for in evaluating overall swimmer performance. While this depends on the specific implementation, piezoelectric materials typically exhibit high efficiency, up to 90 %, in converting electrical energy into mechanical work (Richards *et al.* 2004; Steiger & Mokrỳ 2015; Nabawy & Crowther 2016). Consequently, MFC propulsors can be expected to yield high overall efficiency compared to traditional mechanical propulsors, while providing reduced size, enhanced robustness and operational flexibility.

The performance of propulsors with combined actuation could potentially be further improved by employing more advanced forms of internal actuation, such as segmented MFC actuators with independent control of individual sequential segments. In this scenario, each segment could be used to impose a bending moment, enabling greater control over the dynamics of the propulsor that could be further optimized to mimic fish-like kinematics for enhanced hydrodynamic performance. Furthermore, hybrid propulsors could be used not only for forward propulsion but also for swimmer navigation, by applying asymmetric actuation to the MFCs; this would simplify the design and operation of robotic swimmers. Finally, piezoelectric propulsors could be used to harvest energy from unsteady fluid environments, enabling increased autonomy of robotic swimmers (Yang, Tang & Li 2009; Song *et al.* 2010; Erturk & Inman 2011).

Supplementary material. A supplementary movie and other material are available at https://doi.org/10.1017/jfm.2021.558.

Funding. We thank the National Science Foundation (CBET-1705739) for financial support.

Declaration of interest. The authors report no conflict of interest.

Author ORCIDs.
Ersan Demirer https://orcid.org/0000-0002-9710-6906;
Alexander Alexeev https://orcid.org/0000-0002-8285-0003.

References

Alben, S., Witt, C., Baker, T.V., Anderson, E. & Lauder, G.V. 2012 Dynamics of freely swimming flexible foils. *Phys. Fluids* **24** (5), 051901.

Anderson, J.M., Streitlien, K., Barrett, D.S. & Triantafyllou, M.S. 1998 Oscillating foils of high propulsive efficiency. *J. Fluid Mech.* **360**, 41–72.

Cen, L. & Erturk, A. 2013 Bio-inspired aquatic robotics by untethered piezohydroelastic actuation. *Bioinspir. Biomim.* **8** (1), 016006.

Chen, Z., Shatara, S. & Tan, X. 2009 Modeling of biomimetic robotic fish propelled by an ionic polymer–metal composite caudal fin. *IEEE ASME Trans. Mechatron.* **15** (3), 448–459.

Chen, Z., Um, T.I., Zhu, J. & Bart-Smith, H. 2011 Bio-inspired robotic cownose ray propelled by electroactive polymer pectoral fin. In *ASME 2011 International Mechanical Engineering Congress and Exposition*, pp. 817–824. American Society of Mechanical Engineers Digital Collection.

Chu, W.-S., Lee, K.-T., Song, S.-H., Han, M.-W., Lee, J.-Y., Kim, H.-S., Kim, M.-S., Park, Y.-J., Cho, K.-J. & Ahn, S.-H. 2012 Review of biomimetic underwater robots using smart actuators. *Intl J. Precis. Engng Manuf.* **13** (7), 1281–1292.

Combes, S.A. & Daniel, T.L. 2001 Shape, flapping and flexion: wing and fin design for forward flight. *J. Expl Biol.* **204** (12), 2073–2085.

Dai, H., Luo, H., de Sousa, P.J.S.A.F. & Doyle, J.F. 2012 Thrust performance of a flexible low-aspect-ratio pitching plate. *Phys. Fluids* **24** (10), 101903.

Demirer, E., Wang, Y.-C., Erturk, A. & Alexeev, A. 2021 Effect of actuation method on hydrodynamics of elastic plates oscillating at resonance. *J. Fluid Mech.* **910**, A4.

Erturk, A. & Inman, D.J. 2011 *Piezoelectric Energy Harvesting*. John Wiley & Sons.

Esposito, C.J., Tangorra, J.L., Flammang, B.E. & Lauder, G.V. 2012 A robotic fish caudal fin: effects of stiffness and motor program on locomotor performance. *J. Expl Biol.* **215** (1), 56–67.

Fish, F.E. & Lauder, G.V. 2006 Passive and active flow control by swimming fishes and mammals. *Annu. Rev. Fluid Mech.* **38**, 193–224.

Flammang, B.E. & Lauder, G.V. 2009 Caudal fin shape modulation and control during acceleration, braking and backing maneuvers in bluegill sunfish, *Lepomis macrochirus*. *J. Expl Biol.* **212** (2), 277–286.

Heo, S., Wiguna, T., Park, H.C. & Goo, N.S. 2007 Effect of an artificial caudal fin on the performance of a biomimetic fish robot propelled by piezoelectric actuators. *J. Bionic Engng* **4** (3), 151–158.

Hoover, A.P., Cortez, R., Tytell, E.D. & Fauci, L.J. 2018 Swimming performance, resonance and shape evolution in heaving flexible panels. *J. Fluid Mech.* **847**, 386–416.

Hu, H., Liu, J., Dukes, I. & Francis, G. 2006 Design of 3D swim patterns for autonomous robotic fish. In *2006 IEEE/RSJ International Conference on Intelligent Robots and Systems*, pp. 2406–2411.

Jayne, B.C. & Lauder, G.V. 1995 Speed effects on midline kinematics during steady undulatory swimming of largemouth bass, *Micropterus salmoides*. *J. Expl Biol.* **198** (2), 585–602.

Kolomenskiy, D., Moffatt, H.K., Farge, M. & Schneider, K. 2011 The Lighthill–Weis-Fogh clap–fling–sweep mechanism revisited. *J. Fluid Mech.* **676**, 572–606.

Kopman, V., Laut, J., Acquaviva, F., Rizzo, A. & Porfiri, M. 2015 Dynamic modeling of a robotic fish propelled by a compliant tail. *IEEE J. Ocean. Engng* **40** (1), 209–221.

Ladd, A.J.C. & Verberg, R 2001 Lattice–Boltzmann simulations of particle-fluid suspensions. *J. Stat. Phys.* **104** (5–6), 1191–1251.

Lauder, G.V. & Tangorra, J.L. 2015 *Fish Locomotion: Biology and Robotics of Body and Fin-Based Movements*, pp. 25–49. Springer.

Lauder, G.V. & Tytell, E.D. 2005 Hydrodynamics of undulatory propulsion. *Fish Physiol.* **23**, 425–468.

Li, N., Liu, H. & Su, Y. 2017 Numerical study on the hydrodynamics of thunniform bio-inspired swimming under self-propulsion. *PLoS ONE* **12** (3), e0174740.

LIU, H. & AONO, H. 2009 Size effects on insect hovering aerodynamics: an integrated computational study. *Bioinspir. Biomim.* **4** (1), 015002.

MAO, W. & ALEXEEV, A. 2014 Motion of spheroid particles in shear flow with inertia. *J. Fluid Mech.* **749**, 145–166.

MARRAS, S. & PORFIRI, M. 2012 Fish and robots swimming together: attraction towards the robot demands biomimetic locomotion. *J. R. Soc. Interface* **9** (73), 1856–1868.

MASON, R. & BURDICK, J.W. 2000 Experiments in carangiform robotic fish locomotion. In *Proceedings 2000 ICRA. Millennium Conference. IEEE International Conference on Robotics and Automation. Symposia Proceedings (Cat. No. 00CH37065)*, vol. 1, pp. 428–435. IEEE.

MASOUD, H. & ALEXEEV, A. 2010 Resonance of flexible flapping wings at low Reynolds number. *Phys. Rev.* E **81** (5), 056304.

MASOUD, H. & ALEXEEV, A. 2012 Efficient flapping flight using flexible wings oscillating at resonance. In *Natural Locomotion in Fluids and on Surfaces*, pp. 235–245. Springer.

MCHENRY, M.J., PELL, C.A. & LONG, J.H. 1995 Mechanical control of swimming speed: stiffness and axial wave form in undulating fish models. *J. Expl Biol.* **198** (11), 2293–2305.

MICHELIN, S. & LLEWELLYN SMITH, S.G. 2009 Resonance and propulsion performance of a heaving flexible wing. *Phys. Fluids* **21** (7), 071902.

NABAWY, M.R.A. & CROWTHER, W.J. 2016 Dynamic electromechanical coupling of piezoelectric bending actuators. *Micromachines* **7** (1), 12.

PABST, D.A. 2015 Springs in swimming animals. *Am. Zool.* **36** (6), 723–735.

PHILEN, M. & NEU, W. 2011 Hydrodynamic analysis, performance assessment, and actuator design of a flexible tail propulsor in an artificial alligator. *Smart Mater. Struct.* **20** (9), 094015.

PIÑEIRUA, M., THIRIA, B. & GODOY-DIANA, R. 2017 Modelling of an actuated elastic swimmer. *J. Fluid Mech.* **829**, 731–750.

QUINN, D.B., LAUDER, G.V. & SMITS, A.J. 2014 Scaling the propulsive performance of heaving flexible panels. *J. Fluid Mech.* **738**, 250–267.

QUINN, D.B., LAUDER, G.V. & SMITS, A.J. 2015 Maximizing the efficiency of a flexible propulsor using experimental optimization. *J. Fluid Mech.* **767**, 430–448.

RAMANANARIVO, S., GODOY-DIANA, R. & THIRIA, B. 2011 Rather than resonance, flapping wing flyers may play on aerodynamics to improve performance. *Proc. Natl Acad. Sci.* **108** (15), 5964–5969.

RAMANANARIVO, S., GODOY-DIANA, R. & THIRIA, B. 2013 Passive elastic mechanism to mimic fish-muscle action in anguilliform swimming. *J. R. Soc. Interface* **10** (88), 20130667.

RASPA, V., RAMANANARIVO, S., THIRIA, B. & GODOY-DIANA, R. 2014 Vortex-induced drag and the role of aspect ratio in undulatory swimmers. *Phys. Fluids* **26** (4), 041701.

RICHARDS, C.D., ANDERSON, M.J., BAHR, D.F. & RICHARDS, R.F. 2004 Efficiency of energy conversion for devices containing a piezoelectric component. *J. Micromech. Microeng.* **14** (5), 717.

SMITS, A.J. 2019 Undulatory and oscillatory swimming. *J. Fluid Mech.* **874**, P1.

SODANO, H.A. 2003 Macro-fiber composites for sensing, actuation and power generation. PhD thesis, Virginia Tech.

SONG, H.J., CHOI, Y.-T., WERELEY, N.M. & PUREKAR, A.S. 2010 Energy harvesting devices using macro-fiber composite materials. *J. Intell. Mater. Syst. Struct.* **21** (6), 647–658.

STEIGER, K. & MOKRÝ, P. 2015 Finite element analysis of the macro fiber composite actuator: macroscopic elastic and piezoelectric properties and active control thereof by means of negative capacitance shunt circuit. *Smart Mater. Struct.* **24** (2), 025026.

SU, Z., YU, J., TAN, M. & ZHANG, J. 2014 Implementing flexible and fast turning maneuvers of a multijoint robotic fish. *IEEE ASME Trans. Mechatron.* **19** (1), 329–338.

TAN, D. & ERTURK, A. 2018 On the coupling of nonlinear macro-fiber composite piezoelectric cantilever dynamics with hydrodynamic loads. In *Active and Passive Smart Structures and Integrated Systems XII* (ed. A. Erturk), vol. 10595, pp. 166–174. International Society for Optics and Photonics, SPIE.

TRIANTAFYLLOU, M.S. & TRIANTAFYLLOU, G.S. 1995 An efficient swimming machine. *Sci. Am.* **272** (3), 64–70.

VAN BUREN, T., FLORYAN, D. & SMITS, A.J. 2019 Scaling and performance of simultaneously heaving and pitching foils. *AIAA J.* **57** (9), 3666–3677.

WANG, Z., HANG, G., LI, J., WANG, Y. & XIAO, K. 2008 A micro-robot fish with embedded SMA wire actuated flexible biomimetic fin. *Sens. Actuators* A*: Phys.* **144** (2), 354–360.

WARDLE, C.S.J.J., VIDELER, J. & ALTRINGHAM, J. 1995 Tuning in to fish swimming waves: body form, swimming mode and muscle function. *J. Expl Biol.* **198** (8), 1629–1636.

WEAVER, W. JR., TIMOSHENKO, S.P. & YOUNG, D.H. 1990 *Vibration Problems in Engineering*. John Wiley & Sons.

WILLIAMS, R.B., INMAN, D.J. & WILKIE, W.K. 2006 Nonlinear response of the macro fiber composite actuator to monotonically increasing excitation voltage. *J. Intell. Mater. Syst. Struct.* **17** (7), 601–608.

WU, Z.X., YU, J.Z., SU, Z.S., TAN, M. & LI, Z.L. 2015 Towards an *Esox lucius* inspired multimodal robotic fish. *Sci. China Inf. Sci.* **58** (5), 1–13.

YAN, Q., HAN, Z., ZHANG, S.-W. & YANG, J. 2008 Parametric research of experiments on a carangiform robotic fish. *J. Bionic Engng* **5** (2), 95–101.

YANG, Y., TANG, L. & LI, H. 2009 Vibration energy harvesting using macro-fiber composites. *Smart Mater. Struct.* **18** (11), 115025.

YEH, P.D. & ALEXEEV, A. 2014 Free swimming of an elastic plate plunging at low Reynolds number. *Phys. Fluids* **26** (5), 053604.

YEH, P.D. & ALEXEEV, A. 2016*a* Biomimetic flexible plate actuators are faster and more efficient with a passive attachment. *Acta Mechanica Sin.* **32** (6), 1001–1011.

YEH, P.D. & ALEXEEV, A. 2016*b* Effect of aspect ratio in free-swimming plunging flexible plates. *Comput. Fluids* **124**, 220–225.

YEH, P.D., DEMIRER, E. & ALEXEEV, A. 2019 Turning strategies for plunging elastic plate propulsor. *Phys. Rev. Fluids* **4**, 064101.

YEH, P.D., LI, Y. & ALEXEEV, A. 2017 Efficient swimming using flexible fins with tapered thickness. *Phys. Rev. Fluids* **2**, 102101.

YU, J., TAN, M., WANG, S. & CHEN, E. 2004 Development of a biomimetic robotic fish and its control algorithm. *IEEE Trans. Syst. Man Cybern.* **34** (4), 1798–1810.